

Computational study of the generation of crystal defects in a bcc metal target irradiated by short laser pulses

Zhibin Lin, Robert A. Johnson, and Leonid V. Zhigilei*

Department of Materials Science and Engineering, University of Virginia, 395 McCormick Road, Charlottesville, Virginia 22904-4745, USA

(Received 22 February 2008; revised manuscript received 10 May 2008; published 16 June 2008)

The generation of crystal defects in a Cr target irradiated by a short, 200 fs, laser pulse is investigated in computer simulations performed with a computational model that combines the classical molecular dynamics method with a continuum description of the laser excitation of conduction band electrons, electron-phonon coupling, and electron heat conduction. Interatomic interactions are described by the embedded atom method (EAM) potential with a parametrization designed for Cr. The potential is tested by comparing the properties of the EAM Cr material with experimental data and predictions of density functional theory calculations. The simulations are performed at laser fluences close to the threshold for surface melting. Fast temperature variation and strong thermoelastic stresses produced by the laser pulse are causing surface melting and epitaxial resolidification, transient appearance of a high density of stacking faults along the $\{110\}$ planes, and generation of a large number of point defects (vacancies and self-interstitials). The stacking faults appear as a result of internal shifts in the crystal undergoing a rapid uniaxial expansion in the direction normal to the irradiated surface. The stacking faults are unstable and disappear shortly after the laser-induced tensile stress wave leaves the surface region of the target. Thermally activated generation of vacancy-interstitial pairs during the initial temperature spike and quick escape of highly mobile self-interstitials to the melting front or the free surface of the target, along with the formation of vacancies at the solid-liquid interface during the fast resolidification process, result in a high density of vacancies, on the order of 10^{-3} per lattice site, created in the surface region of the target. The strong supersaturation of vacancies can be related to the incubation effect in multipulse laser ablation/damage and should play an important role in mixing/alloying of multicomponent or composite targets.

DOI: [10.1103/PhysRevB.77.214108](https://doi.org/10.1103/PhysRevB.77.214108)

PACS number(s): 61.80.Ba, 02.70.Ns, 64.70.D-, 61.80.Az

I. INTRODUCTION

Surface modification by laser irradiation is in the core of many modern processing and fabrication techniques, including, e.g., laser surface alloying, annealing, and hardening.¹⁻⁴ The improvement of surface properties is achieved by structural and compositional modification of a surface layer through the formation of metastable phases, grain refinement, generation/annealing of crystal defects, and redistribution of the alloying elements. Recent progress in the development of accessible sources of short (picosecond and femtosecond) laser pulses opens up new possibilities for surface modification with high accuracy and spatial resolution. The shallow depths of the laser energy deposition and steep temperature gradients, typically produced by the short pulse laser irradiation, can result in the confinement of the laser-induced structural modifications within a surface layer as small as tens to hundreds of nanometers.⁵⁻⁸ The small size of the laser-modified zone makes characterization of laser-induced structural changes challenging and, at the same time, increases the importance of understanding of the nucleation, mobility, interactions, and stability of individual crystal defects and their ensembles.

With a quickly expanding range of time and length scales accessible for molecular dynamics (MD) simulations (systems containing $\sim 10^6$ – 10^7 atoms, with sizes on the order of hundreds of nanometers, can be simulated for nanoseconds^{9,10}), the atomistic computer modeling has a good potential of revealing the mechanisms of laser-induced phase and structural transformations. Indeed, MD simula-

tions have been successfully applied for investigation of the microscopic mechanisms of laser melting,¹¹⁻¹³ photomechanical spallation,^{14,15} and ablation^{10,16-20} of metal targets. A detailed analysis of the crystal defects introduced by short pulse irradiation, however, has not been performed in MD simulations so far and the question on the atomic-level mechanisms responsible for the generation and evolution of defect configurations in laser materials processing remains largely unexplored.

In this paper we present the results of MD simulations of short pulse laser interaction with a body-centered-cubic (bcc) metal, Cr. The laser fluences used in the simulations are chosen to be close to the threshold for the onset of surface melting and the main focus of the paper is on the detailed analysis of the crystal defects generated in the surface region of the irradiated bulk target. A long term evolution of subsurface defect configurations is studied and implications for practical applications of nonablative laser surface modification are discussed. A brief description of the computational model used in the simulations is given below, in Sec. II. A parametrization of a computationally efficient embedded atom method (EAM) potential for Cr as well as the physical properties of the model Cr material predicted by the potential are presented in Sec. III. The results of the simulations of a transient surface melting and generation of crystal defects in the surface region of a Cr target irradiated by a femtosecond laser pulse are presented in Sec. IV and summarized in Sec. V.

II. COMPUTATIONAL MODEL FOR LASER INTERACTIONS WITH A Cr TARGET

The simulations of short pulse laser irradiation of a bulk Cr target are performed with a computational model that combines the classical MD method with a continuum description of the laser excitation and subsequent relaxation of the conduction band electrons.¹¹ The model is based on well-known two-temperature model (TTM),²¹ which describes the time evolution of the lattice and electron temperatures by two coupled nonlinear differential equations. In the combined model, the MD method substitutes the TTM equation for the lattice temperature in the surface region of the target, where the laser-induced structural transformations are expected to take place. The diffusion equation for the electron temperature is solved by a finite difference method simultaneously with MD integration of the equations of motion of atoms. The electron temperature enters a coupling term that is added to the MD equations of motion to account for the energy exchange between the electrons and the lattice. The cells in the finite difference discretization are related to the corresponding volumes of the MD system and the local lattice temperature is defined for each cell from the average kinetic energy of thermal motion of atoms.

The hybrid atomistic-continuum model, briefly discussed above, combines the advantages of TTM and MD methods. TTM provides an adequate description of the laser energy deposition into the electronic system, energy exchange between the electrons and phonons, and fast electron heat conduction in metals, whereas the MD representation of the surface region of the target enables atomic-level investigations of laser-induced structural and phase transformations. A complete description of the TTM-MD model is given elsewhere.¹¹ Below we provide the details of the computational setup designed for the simulation of laser interaction with a bulk Cr target.

The MD part of the TTM-MD model represents the top 100 nm surface region of the Cr target and is composed of 630 000 atoms initially arranged in a bcc crystallite with dimensions of $8 \times 8 \times 100$ nm³. Periodic boundary conditions are imposed in the directions parallel to the (100) free surface of the target. At the bottom of the MD computational cell, a dynamic nonreflecting boundary condition^{22,23} is applied to account for the propagation of the laser-induced pressure wave from the surface region of the target represented by the MD method to the continuum part of the model. The energy carried away by the pressure wave is monitored, allowing for control over the total energy conservation in the combined model. In the continuum part of the model, beyond the MD region, the electron heat conduction and the energy exchange between the electrons and the lattice are described by the conventional TTM. The size of the continuum (TTM) region is chosen to be 500 nm, so that no significant changes in the electron and lattice temperatures are observed at the bottom of the continuum region during the time of the simulations.

The thermal and elastic properties of the target material, such as the lattice heat capacity, elastic moduli, coefficient of thermal expansion, melting temperature, volume and entropy of melting and vaporization, etc., are all defined by the inter-

atomic interaction potential, described in this work by EAM in the form presented in Sec. III. The parameters used for Cr in the TTM equation for the electron temperature are as follows. The electronic heat capacity is $C_e = \gamma T_e$, with $\gamma = 194$ J m⁻³ K⁻²,²⁴ the electron-phonon coupling constant is $G = 4.2 \times 10^{17}$ W m⁻³ K⁻¹,²⁵ and the dependence of the electron thermal conductivity on the electron and lattice temperatures is described as $K_e = K_0 T_e / T_l$, with $K_0 = 94$ W m⁻¹ K⁻¹.²⁴ Irradiation by a 200 fs laser pulse is represented through a source term with a Gaussian temporal profile and exponential attenuation of laser intensity with depth under the surface (Beer-Lambert law) added to the TTM equation for the electron temperature. An optical penetration depth of 8.9 nm at a laser wavelength of 400 nm (Ref. 26) is assumed in the simulations and the absorbed laser fluence rather than the incident fluence is used in the discussion of the simulation results. Before applying laser irradiation, the whole computational system is equilibrated at 300 K.

III. EMBEDDED ATOM METHOD INTERATOMIC POTENTIAL FOR Cr

Several potentials based on the modified embedded atom method (MEAM) (Refs. 27–29) have been suggested for bcc transition metals. The parametrizations of MEAM include Cr, which features a negative Cauchy pressure (CP) at low temperatures. Consideration of the angular dependence in the interatomic interactions, however, complicates the implementation of MEAM potentials and makes large-scale MD simulations computationally expensive. In this section we present a reformulation of the EAM potential of Johnson and co-workers^{30,31} for Cr that provides an attractive alternative to MEAM. With a simple analytical functional form and the absence of explicit angular terms, the potential is easy to implement and computationally efficient, making it appropriate for MD simulations that involve large numbers of atoms. Below, the EAM potential and the parametrization for Cr are described. Some of the physical properties of the model EAM Cr material are calculated and related to the experimental data and the predictions of density functional theory (DFT) calculations.

In the EAM formalism, the total potential energy of a system of N atoms is defined as

$$E_{\text{pot}} = \sum_{i=1}^N E_i = \frac{1}{2} \sum_{i=1}^N \sum_{\substack{j=1 \\ j \neq i}}^N \phi_{ij}(r_{ij}) + \sum_{i=1}^N F_i(\rho_i), \quad (1)$$

where E_i is the potential energy of an atom i , $\phi(r_{ij})$ is the pair energy term defined as a function of the interatomic distance r_{ij} between atoms i and j , and $F_i(\rho_i)$ is the many-body embedding energy term defined as a function of the local electron density, ρ_i , at the position of atom i . The local electron density is calculated as a linear sum of the partial electron density contributions from the neighboring atoms,

TABLE I. Parameters of the EAM potential for Cr.

r_e (Å)	f_e (eV/Å)	ρ_e (eV/Å)	ρ_s (eV/Å)	κ
2.493 879	1.793 835	17.641 302	19.605 45	0.185 33
λ	A (eV)	B (eV)	α	β
0.277 995	1.551 848	1.827 556	8.604 593	7.170 494
F_0 (eV)	F_1 (eV)	F_2 (eV)	F_3 (eV)	η
-2.022 754	0.039 608	-0.183 611	-2.245 972	0.456
F_{m0} (eV)	F_{m1} (eV)	F_{m2} (eV)	F_{m3} (eV)	F_n (eV)
-2.02	0	-0.056 517	0.439 144	-2.020 038

$$\rho_i = \sum_{\substack{j=1 \\ j \neq i}}^N f_j(r_{ij}), \quad (2)$$

where $f_j(r_{ij})$ is the contribution from atom j to the electron density at the site of the atom i .

The functional form of the EAM Cr is similar to the one suggested in Ref. 31. The pair energy term is defined as

$$\phi(r) = \frac{A \exp\left[-\alpha\left(\frac{r}{r_e} - 1\right)\right]}{1 + \left(\frac{r}{r_e} - \kappa\right)^{20}} - \frac{B \exp\left[-\beta\left(\frac{r}{r_e} - 1\right)\right]}{1 + \left(\frac{r}{r_e} + \lambda\right)^{20}}, \quad (3)$$

the electron density function is

$$f(r) = \frac{f_e \exp\left[-\beta\left(\frac{r}{r_e} - 1\right)\right]}{1 + \left(\frac{r}{r_e} - \lambda\right)^{20}}, \quad (4)$$

and the embedding energy function is represented by three equations defining the function in different electron density ranges and having matching values and slopes at the two junctions,

$$F(\rho) = \sum_{i=0}^3 F_i \left(\frac{\rho}{0.85\rho_e} - 1\right)^i, \quad \rho < 0.85\rho_e,$$

$$F(\rho) = \sum_{i=0}^3 F_{mi} \left(\frac{\rho}{\rho_e} - 1\right)^i, \quad 0.85\rho_e < \rho < 1.15\rho_e,$$

$$F(\rho) = F_n \left[1 - \eta \ln\left(\frac{\rho}{\rho_s}\right)\right] \left(\frac{\rho}{\rho_s}\right)^\eta, \quad \rho > 1.15\rho_e. \quad (5)$$

The parameters of the potential for Cr are given in Table I. They are obtained by fitting to the experimental equilibrium lattice constant of 2.88 Å,²⁴ the cohesive energy of 4.10 eV,²⁴ the vacancy formation energy of 2.08 eV,³² the bulk modulus $B=(C_{11}+2C_{12})/3$ of 194.8 GPa,³³ the Voigt average shear modulus $G=(3C_{44}+2C')/5$ of 123 GPa,³³ and the anisotropy ratio C_{44}/C' of 0.68,³³ where C_{44} and $C'=(C_{11}-C_{12})/2$ are the two shear moduli of the cubic crystal.

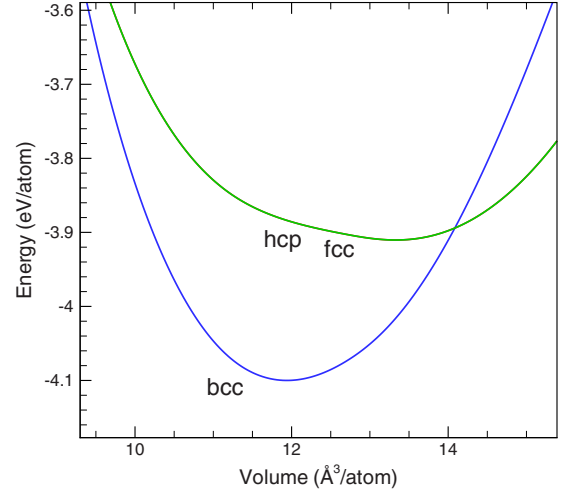


FIG. 1. (Color online) Total energy at zero temperature as a function of atomic volume predicted by the EAM Cr potential for bcc, fcc, and hcp crystal structures. The energy difference between the fcc and hcp structures is so small that the plots for these two structures cannot be visually distinguished.

There is no explicit cutoff distance in the potential functions, but the pair energy term and the electron density function are vanishing beyond the third neighbor shell in the Cr bcc structure (the contribution from the fourth neighbors to the interaction energy is 2 orders of magnitude smaller than that from the third neighbors).

The energies of bcc, fcc, and hcp crystal structures calculated with the EAM Cr potential are shown in Fig. 1 as functions of atomic volume. The bcc lattice remains the lowest energy structure for large variations around the equilibrium volume, up to more than 15% expansion and even larger compression. The short range of the interactions contributing to the EAM Cr potential and the similarity of the local atomic structure results in a very small energy difference between the two close-packed structures.

The temperature dependences of the elastic constants are calculated for EAM Cr using the statistical fluctuation method suggested in Ref. 34 and widely used to obtain finite temperature values of elastic constants in MD simulations performed with many-body potentials.³⁵⁻³⁷ The calculations of the elastic constants for EAM Cr are performed with a MD cell containing 2000 atoms arranged in a bcc structure and periodic boundary conditions applied in all directions. After equilibration of the system at a given temperature and constant zero pressure, a constant energy and constant volume simulation is carried out and the elastic constants are calculated using the statistical fluctuation method. The convergence of the calculations is ensured by collecting statistics over sufficiently long MD trajectories, 200 ps. Results of the calculations of the temperature dependences of the two shear moduli, C_{44} and C' , and the bulk modulus are shown and compared with experimental values in Fig. 2. While there are no experimental measurements reported for elastic constants above 700 K, a reasonable agreement between the values and trends in the temperature dependences predicted with the EAM Cr potential and experimental data^{33,38} is found up to 700 K. The EAM Cr potential also correctly reproduces the

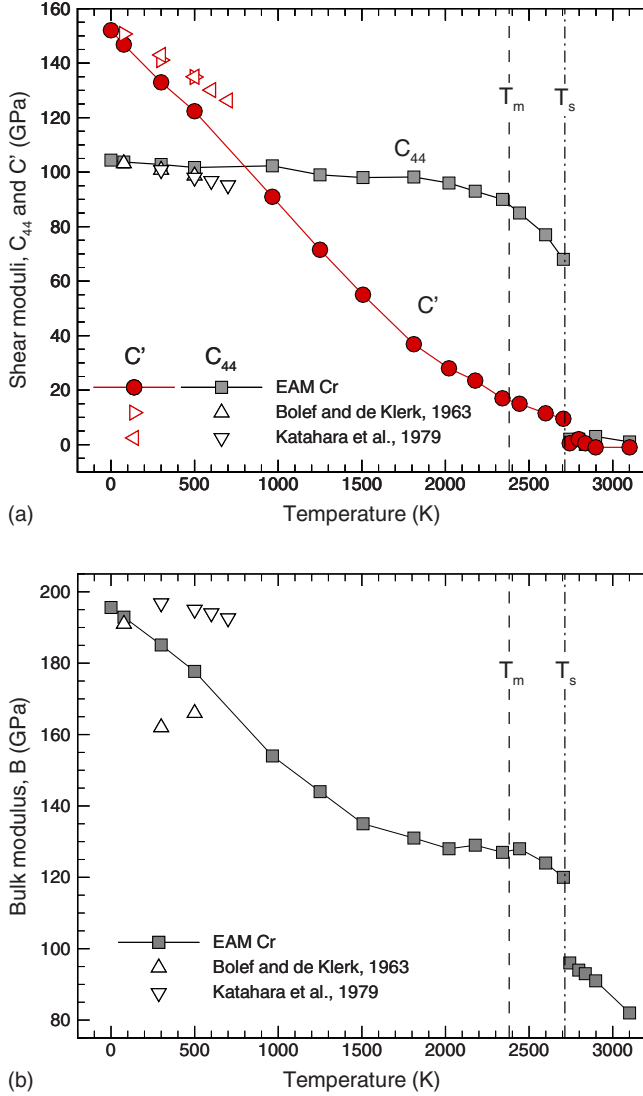


FIG. 2. (Color online) Temperature dependences of (a) two shear moduli, C_{44} and C' , and (b) bulk modulus B calculated with the EAM Cr potential, along with experimental data from Refs. 33 and 38. The vertical dashed and solid lines are marking the equilibrium melting temperature T_m and the maximum superheating temperature T_s , calculated for EAM Cr.

negative sign of the Cauchy pressure $CP=B-5/3G=C_{12}-C_{44}$, which is determined to be -10.2 GPa at 0 K and -6.3 GPa at 300 K.

Some other properties of the EAM Cr material, relevant to the laser heating/melting simulations presented in this paper, are listed in Table II, along with experimental data for Cr and the predictions of the MEAM potential.²⁷ A series of constant temperature and constant zero pressure simulations is performed to determine the temperature dependence of volume and internal energy of the model material, with the values of heat capacity and coefficient of thermal expansion calculated from slopes of these dependences.¹¹ The equilibrium melting temperature, $T_m=2381 \pm 3$ K (with the error of 3 K corresponding to 95% confidence interval), is determined from a liquid-crystal coexistence simulation performed at zero pressure for a system consisting of 4000 atoms ($3.0 \times 3.0 \times 5.8$ nm³), with liquid-crystal interface oriented along (100) plane of the bcc crystal. The method used to calculate the vacancy migration energy is described in Sec. IV D. The predicted thermophysical properties show a good agreement with experimental data. In particular, the equilibrium melting temperature and the enthalpy of melting of the EAM Cr material are within 10% of the experimental values.

The steady decrease in the shear modulus C' with increasing temperature and the fast drop of C_{44} at temperatures exceeding the equilibrium melting temperature [Fig. 2(a)] can be related to the interpretation of the homogeneous melting at the limit of lattice superheating in terms of the elastic shear instability facilitated by the diminishing shear moduli.⁴²⁻⁴⁵ The temperature that corresponds to the superheating limit of the EAM Cr has been determined to be 2714 K, $\sim 14\%$ above the equilibrium melting temperature. The limit of superheating is defined as the maximum temperature at which no melting is observed within 300 ps in simulation of slow incremental heating performed at zero pressure. The value of the maximum superheating is smaller than typical values reported for close-packed metals (19%–30%) (Ref. 46) but is in agreement with the value of 13% determined for bcc EAM vanadium.⁴⁴ While the shear moduli are not vanishing as the temperature approaches the limit of superheating ($C'=9.5$ GPa and $C_{44}=64$ GPa at 2714 K), the value of C' is small enough to allow for the local destabilization of the lattice and the onset of homogeneous melting. This

TABLE II. Some of the material properties determined for the EAM Cr material. Values of the equilibrium melting temperature, T_m , enthalpy of melting, ΔH_m , and volume change on melting, $\Delta V_m/V_{solid}$, are given for zero pressure. The coefficient of linear expansion, α , and heat capacity at zero pressure, C_p , predicted with EAM Cr and MEAM Cr (Ref. 27) potentials are given for 300 K. Variations of the experimental coefficient of linear expansion and heat capacity are given for zero pressure and a temperature range from 300 to 1000 K. The experimental values are from Ref. 39 for T_m and ΔH_m , from Ref. 40 for C_p , from Ref. 41 for α , and from Ref. 32 for vacancy migration energy, E_v^m .

Properties	T_m (K)	ΔH_m (kJ mol ⁻¹)	$\Delta V_m/V_{solid}$ (%)	C_p (J K ⁻¹ mol ⁻¹)	α (10 ⁻⁶ K ⁻¹)	E_v^m (eV)
EAM Cr	2381	22.6	7.0	26.3	8.2	0.81
Experiment	2180	21.0	N/A	24.0–32.0	6.5–12.0	0.95
MEAM Cr ^a	2050	18.8	4.4	26.8	9.0	0.70

^aReference 27.

mechanism of local “mechanical” melting has been suggested based on the results of recent MD simulations.^{43,45} The generation of vacancy-interstitial pairs and the interactions among the point defects are likely to facilitate the generation of the lattice instabilities.^{44,48,49} Moreover, it has been shown in Ref. 45 that the generation of vacancy-interstitial pairs makes positive contributions to the values of the elastic moduli, suggesting that the change in slope of the temperature dependence of C' and B at high temperatures can be, at least partially, attributed to the rapid increase in the density of the point defects generated at temperatures approaching and exceeding the equilibrium melting temperature.

IV. TTM-MD SIMULATIONS: RESULTS AND DISCUSSION

In this section, the conditions leading to the transient and permanent structural changes in a surface region of a Cr target irradiated by a femtosecond laser pulse are discussed based on the results of two large-scale TTM-MD simulations. The results from a simulation performed at an absorbed laser fluence of 638 J/m^2 , just above the threshold for surface melting, are presented first, followed by a brief discussion of the second simulation performed at a lower absorbed fluence of 425 J/m^2 , when no permanent structural changes are observed in the target at the end of the simulation.

A. Laser-induced stresses, surface melting

The temporal and spatial evolution of the lattice temperature⁴⁷ and pressure in the surface region of a bulk Cr target irradiated by a 200 fs pulse at an absorbed fluence of 638 J/m^2 are shown in the form of contour plots in Fig. 3. The low electronic heat capacity of Cr results in a sharp spike of the electron temperature and a strong electron temperature gradient established in the surface region of the irradiated target immediately after the laser energy deposition. This, in turn, provides the conditions for the fast spread of the laser energy absorbed within the optical penetration depth throughout a deeper surface region of the target during the first 2–3 ps after the pulse. At the same time, the electron-phonon coupling leads to the energy transfer from the hot electrons to the lattice vibrations, as reflected by the initial lattice temperature increase throughout the 150 nm surface region of the target shown in Fig. 3(a). The lattice temperature at the surface of the target, shown in Fig. 4, exceeds the equilibrium melting temperature of the model EAM Cr material, 2381 K, by the time of 3 ps and reaches its maximum level of 2650 K by the time of 5 ps. The initial lattice heating turns into cooling when the electron temperature drops below the lattice temperature due to the fast electron heat conduction to the bulk of the target.

The level of overheating (maximum of $1.11T_m$ at the surface) is not sufficient to trigger the homogeneous nucleation of liquid regions in the overheated part of the target^{11–13} and the melting proceeds by the propagation of the melting front from the surface. The melting front reaches a depth of $\sim 3 \text{ nm}$ by the time of 22 ps, when the surface lattice temperature drops below the equilibrium melting temperature

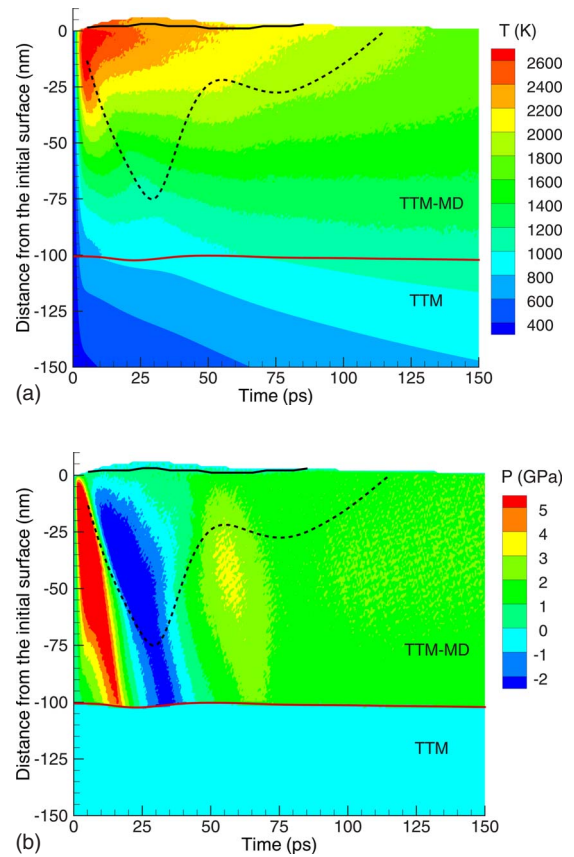


FIG. 3. (Color online) Contour plots of the spatial and temporal evolution of (a) temperature and (b) pressure in a TTM-MD simulation of a bulk Cr target irradiated with a 200 fs laser pulse at an absorbed fluence of 638 J/m^2 . The laser pulse is directed along the Y axes from the top of the contour plots. The red solid line separates the continuum (TTM) and atomistic (TTM-MD) parts of the computational system. The black dashed line marks the depth of the region where stacking faults are observed. The black solid line separates the transiently melted surface region from the crystalline bulk of the target.

and the melting turns into resolidification. The release of the latent heat of melting upon the epitaxial crystallization of the surface region partially offsets the cooling due to the electron heat conduction, leading to the increasing split of the electron and lattice temperatures (Fig. 4). In particular, the release of the latent heat of melting at the crystal-liquid interface stabilizes the lattice temperature of the top 1 nm surface layer at about 2140 K from 60 to 80 ps, when the resolidification front approaches the surface. Similarly to the observation in an earlier investigation of surface melting and resolidification,⁵⁰ the time when the resolidification front reaches the surface of the target, 85 ps, is signified by a spike of the lattice temperature of the top surface layer up to 2190 K.

The split between the electron and the lattice temperatures (Fig. 4) is reflecting the fast rates of the electron cooling due to the steep temperature gradient and the lattice heating due to the release of the latent heat of melting in the resolidification process, as well as the finite time needed for the electron-phonon equilibration. A reverse effect, when the lat-

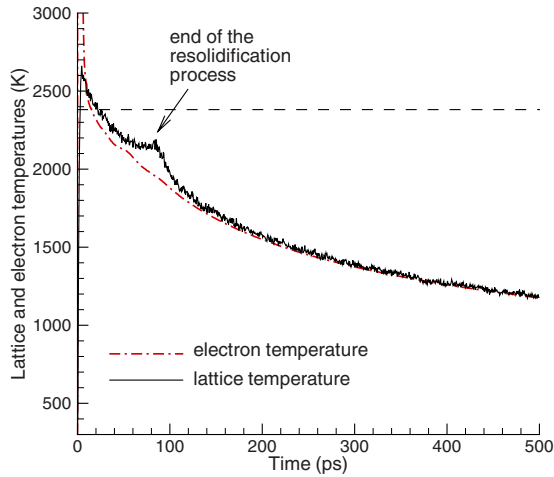


FIG. 4. (Color online) Time dependence of the electron temperature (dash-dotted red line) and lattice (solid black line) temperatures of the top 1 nm surface layer of a bulk Cr target irradiated with a 200 fs laser pulse at an absorbed fluence of 638 J/m^2 , as predicted in a TTM-MD simulation. The horizontal dashed line shows the equilibrium melting temperature of the model EAM Cr material, 2381 K. The lattice temperature is calculated from the average kinetic energy of atoms in the top layer of the sample and the statistical fluctuations of the temperature value are related to the finite number of atoms used in the calculation (1 nm layer of the original sample consists of 6244 atoms).

tice temperature drops significantly below the electron temperature, has been observed for the melting process, where the velocity of the melting front is found to be strongly affected by the local electron-phonon nonequilibrium.⁵¹ The split between the electron and lattice temperatures is larger for metals with weaker electron-phonon coupling.

The fast temperature increase, occurring under conditions of the inertial stress confinement,¹⁴ leads to the compressive pressure buildup in the surface region of the irradiated target [Fig. 3(b)]. The compressive stresses increase during the time of the lattice heating and reach a maximum value of $\sim 11 \text{ GPa}$ at a depth of 16 nm by the time of 3 ps after the laser excitation. The compressive stresses relax by driving a compressive stress wave deeper into the bulk of the target and inducing an unloading tensile wave that follows the compressive component [Fig. 3(b)]. The pressure-transmitting heat-conductive boundary condition, applied at the depth of 100 nm, ensures that both the compressive and tensile components of the pressure wave propagate without any noticeable reflection from the boundary separating the TTM-MD and TTM parts of the model [Fig. 3(b)], whereas the temperature field exhibits a seamless transition at the boundary [Fig. 3(a)].

In addition to the strong pressure wave propagating to the bulk of the target, the laser heating generates an elevated level of the compressive stresses in the surface region of the target. The quasistatic compressive stresses of $\sim 1.5\text{--}2 \text{ GPa}$, observed in Fig. 3(b) long after the relaxation of the initial transient stresses, are related to the confinement of the heated crystalline material in the lateral directions.¹⁴ For a typical laser spot diameter of $\sim 100 \mu\text{m}$, the fast relaxation of the laser-induced thermoelastic stresses can only proceed in the

direction normal to the surface. These conditions of lateral confinement are correctly reproduced by the periodic boundary conditions applied in the directions parallel to the surface. The uniaxial expansion of the surface region of the target results in anisotropic lattice deformations and corresponding anisotropic stresses that remain in the crystalline part of the target as long as the temperature gradients persist in the irradiated target. The value of pressure, shown in Fig. 3(b), is defined as $-1/3$ of the first invariant of the stress tensor, $P = -(\sigma_{xx} + \sigma_{yy} + \sigma_{zz})/3$, and contains contributions mainly from the first two diagonal components of the stress tensor, σ_{xx} and σ_{yy} , with the third component, σ_{zz} , fluctuating around zero. For example, the instantaneous quasistatic compressive pressure of 1.88 GPa measured at a depth of 50 nm at 150 ps contains contributions from $\sigma_{xx} = \sigma_{yy} = -2.91 \text{ GPa}$ and $\sigma_{zz} = 0.18 \text{ GPa}$. The temperature at this depth and time is 1518 K, the lattice parameter in lateral (x and y) directions is fixed at its room-temperature value of 0.288 nm, whereas the lattice parameter in the z direction is 0.298 nm. In the thin transiently melted surface layer, the stresses become isotropic and zero pressure quickly establishes [Fig. 3(b)].

B. Transient generation of stacking faults

A visual inspection of the snapshots of atomic configurations taken at different times of the simulation can serve as a starting point in the analysis of the laser-induced structural changes in the target. In order to reduce the thermal noise in atomic positions and energies, each configuration is quenched for 2 ps using a velocity dampening technique, where the velocity of each individual atom is set to zero at the time when the kinetic energy of the atom maximizes. The fast quenching does not introduce any structural changes to the atomic configurations but makes the visual analysis more straightforward. In the snapshots shown in Fig. 5, the atoms are colored according to their potential energies, from dark blue used for atoms with energy characteristic of the original bcc structure to light blue, green, and red corresponding to increasingly higher potential energies. In this coloring scheme, the transient melting of the surface region discussed above and shown by a black line in Fig. 3 shows up as a red layer that disappears (reduces to a plane composed of atoms located at the surface of the recrystallized target) by the time of 90 ps.

Prominent features of the snapshots shown in Fig. 5 are the appearance, expansion (up to 30 ps), retraction, and disappearance (by 110 ps) of a complex pattern of stripes composed of atoms with elevated potential energy. A detailed analysis of the atomic configurations indicates that most of the atoms with elevated potential energy belong to pairs of atomic planes with crystallographic orientations of $(0\bar{1}1)$, (011) , $(10\bar{1})$, and (101) . These pairs of atomic planes correspond to the stacking faults outlining the regions of the crystal shifted with respect to each other by a displacement vector $a/8\langle 110 \rangle$, where a is the lattice constant. An example of the atomic configurations that includes stacking faults along the (101) plane is shown in Fig. 6(a). Four consecutive (101) planes are shown in this figure, with a lower right part of the crystal displaced down by a vector $a/8[10\bar{1}]$ along (101)

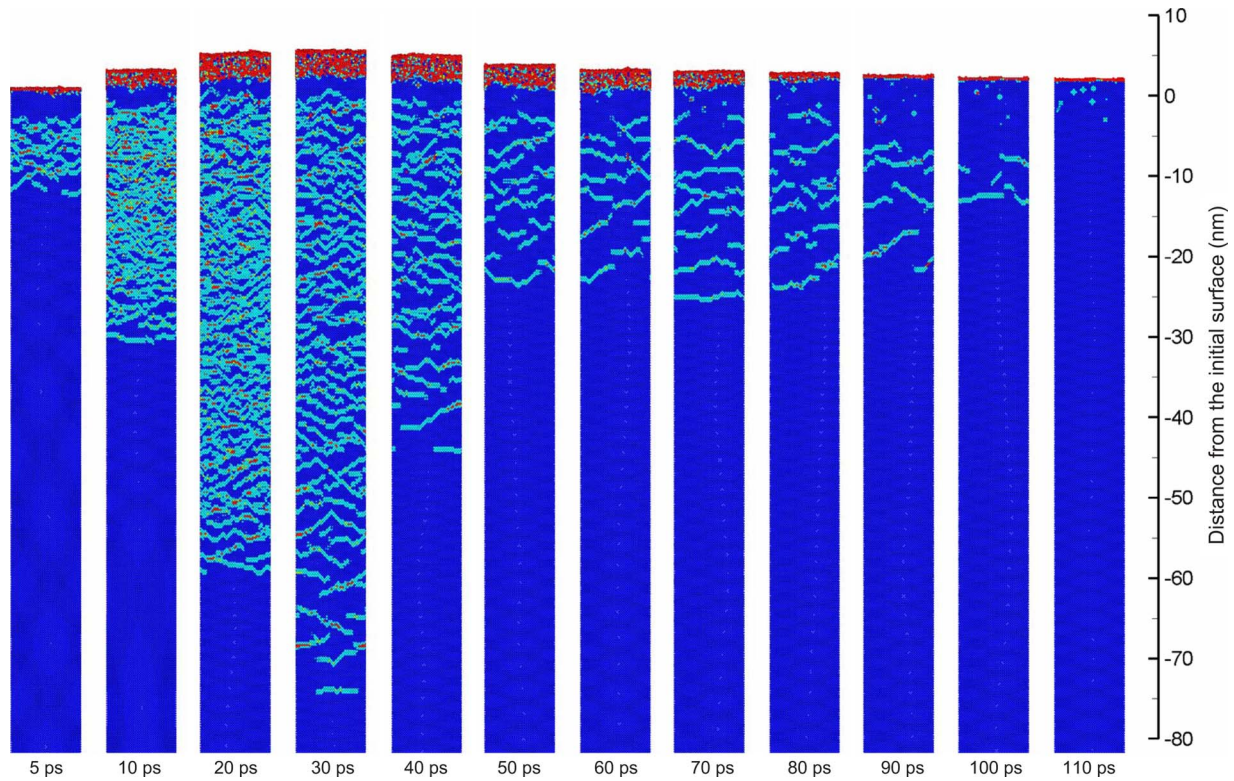


FIG. 5. (Color online) Snapshots of atomic configurations obtained in a TTM-MD simulation of a bulk Cr target irradiated with a 200 fs laser pulse at an absorbed fluence of 638 J/m^2 . The snapshots are taken along the $[010]$ view direction. The configurations are quenched to 0 K in order to reduce thermal noise in atomic positions and energies. Atoms are colored according to their potential energies, from dark blue color corresponding to the energies below -3.99 eV to red color corresponding to the energies above -3.9 eV . This coloring scheme shows the atoms that belong to the original bcc structure in dark blue, the melted surface region in red, and the crystal defects in light blue, green, and red. Enlarged views of the surface parts of these snapshots with low-energy bcc atom blanked are shown in Fig. 8.

planes with respect to the surrounding lattice. The areas of stacking fault are the areas where two atomic planes are displaced with respect to each other, e.g., planes II and III in Fig. 6(a).

The stacking fault discussed above and illustrated in Fig. 6(a) has been analyzed based on the hard-sphere model,⁵² where shifts of parts of a crystal along the $\{110\}$ planes by displacement vectors $a/8\langle 110 \rangle$ bring atoms to local energy minima, as schematically illustrated in Fig. 6(b). Analysis of the stability of this intrinsic stacking fault predicted by the hard-sphere model, however, has revealed that it is unstable if an interatomic potential appropriate for bcc crystals is used in the calculations.^{53,54} It has also been suggested⁵⁴ that an expansion of the crystal may reduce the interatomic interactions beyond the first nearest neighbors and stabilize the stacking faults.

To provide a background for quantitative interpretation of the laser-induced generation of the stacking faults, we perform calculation of the generalized stacking fault energy for the EAM Cr potential. The generalized stacking fault energy is calculated in a simulation performed with a computational cell consisting of 4394 atoms. Following the approach discussed in Ref. 53, the stacking fault is created by dividing the system into two parts by a (100) plane and shifting one part with respect to another in the $[\bar{1}01]$ direction in small increments. After each incremental displacement, the atoms

are allowed to relax in the direction perpendicular to the (100) slip plane using the energy minimization method. After the relaxation, the generalized stacking fault energy is obtained by dividing the energy difference between the displaced system and the perfect lattice by the area of the slip plane. In order to investigate the effect of the laser-induced uniaxial expansion of the lattice on the generalized stacking fault energy, a similar set of simulations is performed for the lattice expanded in the $[001]$ direction. In these simulations the displacement vector that defines the generalized stacking fault is $\vec{u} = X \times [\bar{1}, 0, 1 + \alpha]$, where α is the uniaxial strain applied to the bcc lattice in the $[001]$ direction and X is the ratio of the generalized stacking fault vector \vec{u} to the magnitude of vector $[\bar{1}, 0, 1 + \alpha]$.

The result of the calculation of the generalized stacking fault energy curves is shown in Fig. 7. There are no local minima in the curves obtained for the strain-free bcc lattice, confirming that, in agreement with earlier studies,^{53,54} any stacking fault generated by a displacement in a $\langle 110 \rangle$ direction along a $\{110\}$ plane is unstable in the EAM Cr material. The uniaxial expansion, however, decreases the generalized stacking fault energy and creates a plateau in the vicinity of $X \approx 1/8$. In particular, the GSF energy at $X = 1/8$ decreases from 0.360 J/m^2 at $\alpha = 0$ to 0.352 J/m^2 at $\alpha = 0.01$, to 0.175 J/m^2 at $\alpha = 0.05$, and to 0.093 J/m^2 at $\alpha = 0.07$. The development of the plateau, and even a shallow local mini-

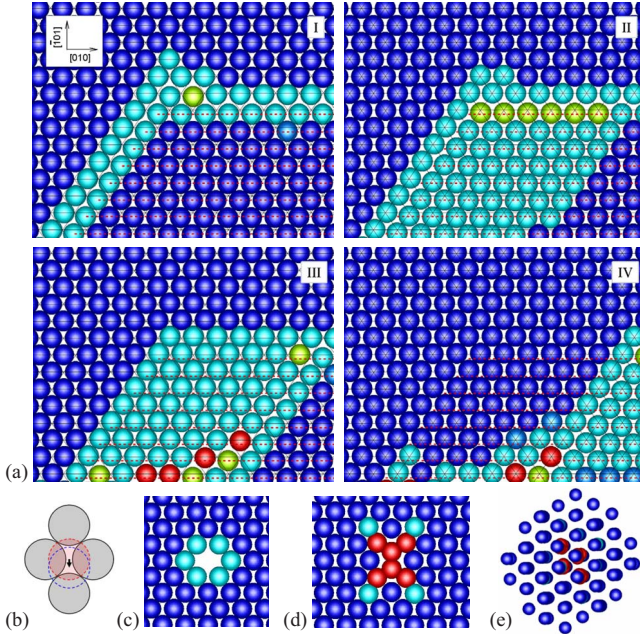


FIG. 6. (Color online) Close up on the atomic arrangements that correspond to the crystal defects observed in the TTM-MD simulation and identified in Fig. 8. A region marked by “A” in a snapshot shown for 100 ps in Fig. 8 is illustrated in (a), where four consecutive (101) planes are shown. This region includes a part (lower right) of the crystal displaced down by a vector $a/8[10\bar{1}]$ along a (101) plane with respect to the original crystal structure. The displacement leads to the formation of stacking faults that show up in the figure as pairs of atomic planes (e.g., II and III) with elevated potential energy. The red dashed lines mark the displaced rows of atoms in plane (II). This type of displacement results in the formation of stacking faults along the $\{110\}$ planes as illustrated by an atomic arrangement in (b), where the displacement of a top atom (dashed circles) is shown by an arrow with respect to four atoms in the underlying (101) plane (solid circles). Atomic configurations that correspond to the defects marked by “B,” “C,” and “D” in a snapshot shown for 450 ps in Fig. 8 are illustrated in (c) a vacancy, (d) an interstitial in a $\langle 110 \rangle$ -dumbbell configuration, and (e) a cluster of four interstitials arranged in a $\langle 111 \rangle$ -crowdion configuration, respectively. A single (101) plane is shown in (c) and (d), and all atoms in the vicinity of the four $\langle 111 \rangle$ -crowdion interstitial cluster that have potential energy higher than -4.09 eV are shown in (e), where the view direction is slightly tilted with respect to the $[\bar{1}11]$ direction. Atoms are colored according to their potential energies, from dark blue color corresponding to the energies below -3.99 eV (these atoms are blanked in Fig. 8) to red color corresponding to the energies above -3.9 eV. The cohesive energy of the EAM Cr bcc crystal is 4.10 eV.

mum observed at 7% strain, suggests that the stacking fault at $X \approx 1/8$, predicted with the hard-sphere model, can be stabilized by the laser-induced uniaxial expansion of the target. Indeed, the analysis of the atomic configurations shown in Fig. 5 suggests that the uniaxial strain reaches its maximum value of 6.5% by the time of 20 ps at a depth of ~ 50 nm below the surface.

The analysis of the stacking fault energy provided above is consistent with the results of the simulations of laser irradiation of a Cr target, where the transient appearance of the

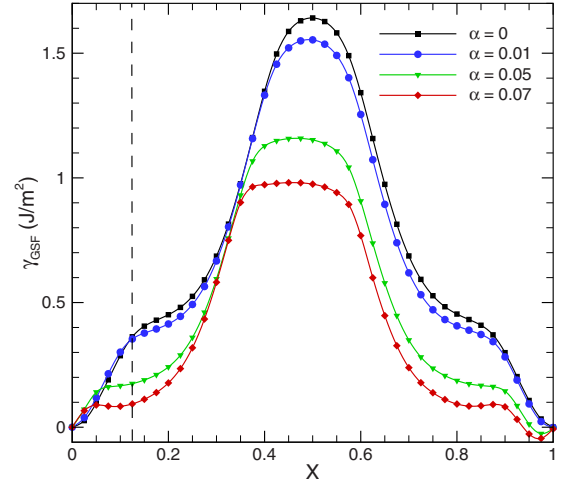


FIG. 7. (Color online) Generalized stacking fault energy, γ_{GSF} , for the (100) slip plane in bcc EAM Cr as a function of the magnitude of the fault vector, $\vec{u} = X \times [\bar{1}, 0, 1 + \alpha]$. The GSF curves are calculated for different values of the uniaxial strain, α , applied to the bcc lattice in the [001] direction. The dashed line marks the stacking fault at $X = 1/8$, predicted with the hard-sphere model.

stacking faults can be clearly correlated with the expansion of the lattice associated with the propagation of the tensile component of the laser-induced stress wave. Indeed, the spreading of the region where the stacking faults are observed (shown by the dashed line in Fig. 3) follows closely the propagation of the tensile stress wave [Fig. 3(b)]. The uniaxial expansion of the lattice in the [001] direction activates multiple shifts in four out of six $\{110\}$ crystallographic planes oriented at 45° with respect to the [001] axis of expansion, namely, $(0\bar{1}1)$, (011) , $(10\bar{1})$, and (101) . The intersections of these planes with the (010) view plane in Fig. 5 are seen as stripes oriented in three directions (horizontal and tilted by $\pm 45^\circ$ with respect to the horizontal direction). The stacking faults on the $\{110\}$ planes start to disappear as soon as the tensile stress wave leaves the surface region and the lattice expansion partially relaxes. The second, much weaker pressure oscillation in the surface region, occurring at around 40–90 ps, is also affecting the evolution of the stacking faults, with the stacking fault region experiencing a small additional growth during the time interval when the lattice expands from 65 to 90 ps [see Fig. 3(b) and snapshots for 60–90 ps in Fig. 5]. As discussed above, this additional lattice expansion takes place on the background of quasistatic thermoelastic stresses defined by the lateral confinement of the lattice and does not result in the negative pressure values. The stacking faults continue to withdraw at later times and completely disappear by the time of 115 ps.

The correlation between the tensile stresses and the appearance of the stacking faults can be further illustrated by the virtual absence of the stacking faults in the top ~ 5 nm part of the target, where the tensile stresses are low [Fig. 3(b)]. The stacking fault-free region can be seen in the snapshots shown in Fig. 5, as well as in the enlarged views of the surface part of the irradiated target, shown in Fig. 8, where the low-energy bcc atoms are blanked in order to expose the crystal defects and the view direction is changed to $[\bar{1}\bar{1}0]$.

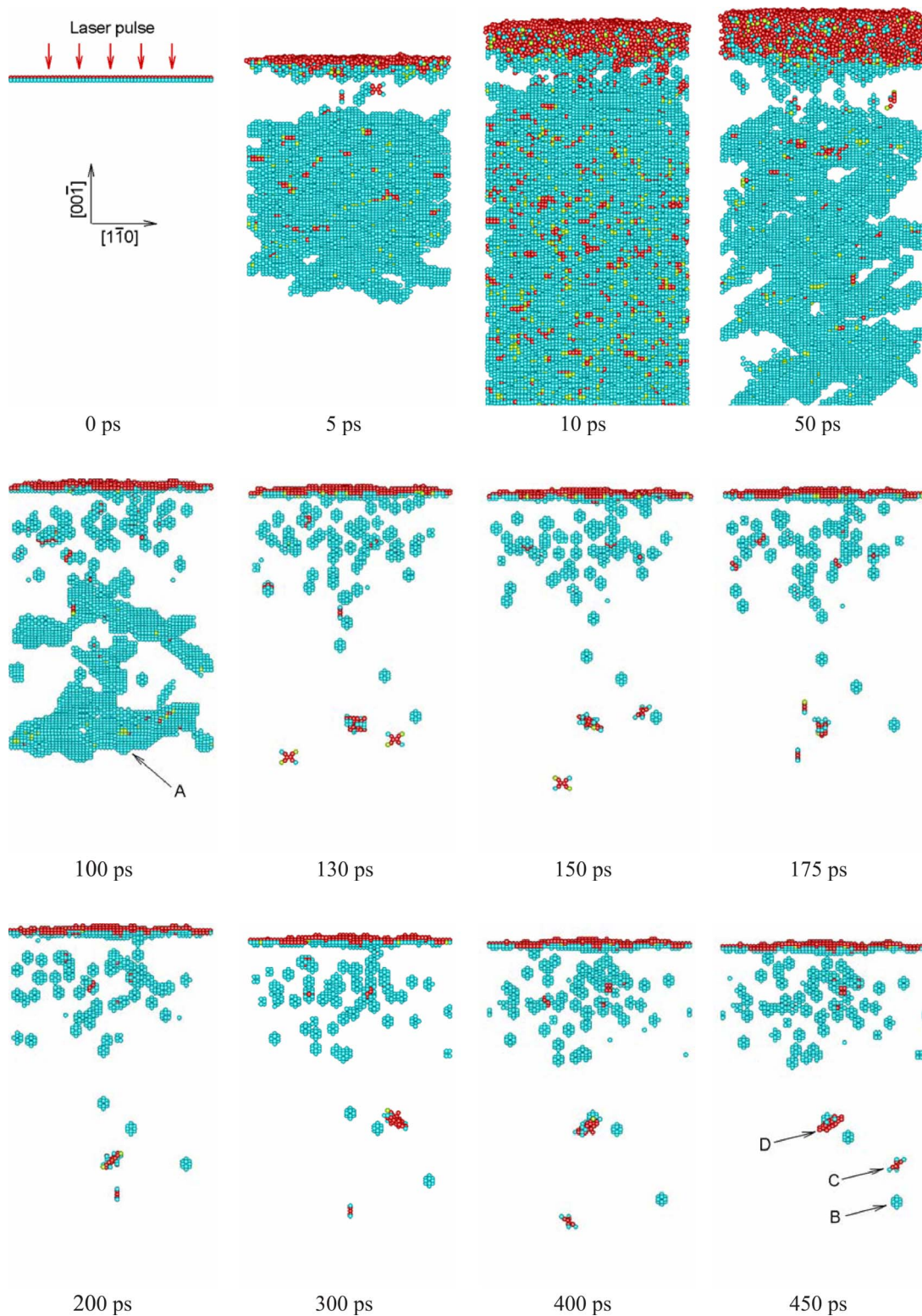


FIG. 8. (Color online) Snapshots of the surface regions of atomic configurations obtained in a TTM-MD simulation of a bulk Cr target irradiated with a 200 fs laser pulse at an absorbed fluence of 638 J/m^2 . The snapshots are taken along the $[\bar{1}\bar{1}0]$ view direction and are shown down to the depth of 20 nm below the level of the initial surface. The configurations are quenched to 0 K in order to reduce thermal noise in atomic positions and energies. The same coloring scheme as in Fig. 5 is used here, with atoms that have energies below -3.99 eV (shown in dark blue in Fig. 5) blanked to expose crystal defects. The red atoms in the top parts of the snapshots belong to the melted region (5, 10, and 50 ps) or are located at the surface of the crystalline target (0 and 100–450 ps). Typical defect configurations marked by A in a snapshot shown for 100 ps and B, C, and D in a snapshot shown for 450 ps correspond to a stacking fault, a vacancy, an interstitial, and a cluster of four interstitials, respectively. The atomic arrangements corresponding to these defects are shown in Fig. 6.

C. Generation of vacancies and self-interstitials

The inspection of Fig. 8 indicates that a large number of point defects are generated by the laser irradiation and many of the defects still remain in the surface region of the target after the disappearance of the stacking faults. Analysis of the atomic configurations reveals that the defects are vacancies, interstitials, divacancies, and a cluster of interstitials. With the visualization method used in Fig. 8, when only atoms with elevated potential energy are shown in the quenched configurations, each vacancy shows up as a cluster of 14 atoms that includes the eight nearest neighbors and six second-nearest neighbors of the missing atom. A closeup on an atomic arrangement around a vacancy is shown in Fig. 6(c), where a single (101) plane is shown. Four out of eight nearest neighbors and two out of six second-nearest neighbors are located in this plane and are shown in light blue color. The individual interstitials are found to always take a $\langle 110 \rangle$ -dumbbell configuration, which is illustrated in Fig. 6(d). In Fig. 8, the interstitials appear as planar crosslike configurations with red atoms in the middle, oriented in one of the $\{110\}$ planes. The $\langle 110 \rangle$ -dumbbell configuration has been predicted to be the most stable self-interstitial configuration in calculations performed for many bcc metals with pairwise⁵⁵ and EAM (Ref. 56) potentials. The energies of the relaxed $\langle 110 \rangle$ and $\langle 111 \rangle$ self-interstitial configurations predicted by the EAM Cr potential used in this work are 5.02 and 5.89 eV, respectively. Recent DFT calculations^{57–59} predict similar values for the formation energies of different self-interstitial configurations, in the range of 5.66–5.85 eV, suggesting that $\langle 110 \rangle$ and $\langle 111 \rangle$ configurations are almost degenerate.⁵⁹ The MEAM Cr potential, however, predicts the $\langle 110 \rangle$ -dumbbell configuration to be the stable one, with a smaller formation energy of 3.9 eV.²⁷

The appearance of point defects can be seen as early as 5 ps after the laser pulse; e.g., two vacancy-interstitial pairs can be identified close to the surface in a snapshot shown for 5 ps in Fig. 8. Due to a much higher mobility of interstitials as compared to vacancies, most of the interstitials quickly diffuse and escape to the melting front or the surface of the target, leaving behind a high concentration of vacancies in the near-surface region. By the time of 150 ps there are only two interstitials located 12.7 and 17 nm below the surface and one cluster of three interstitials located 13.3 nm below the surface. There are no interstitials by this time in the top 10 nm region of the target, and the atoms of high potential energy (shown in red) observed in the top half of Fig. 8 belong to the configurations where two vacancies are located close to each other. Between 175 and 200 ps one of the interstitials joins the cluster, increasing the number of interstitials in the cluster from 3 to 4. Both the three- and four-interstitial clusters have $\langle 111 \rangle$ -crowdion configurations, illustrated in Fig. 8(e) for the four-interstitial cluster. This observation is consistent with earlier results^{60–62} suggesting that small clusters of interstitials arrange themselves into sets of $\langle 111 \rangle$ crowdions/dumbbells. At a sufficiently large size, a $\langle 111 \rangle$ -crowdion cluster can be described as a dislocation loop with a Burgers vector $a/2\langle 111 \rangle$. The high mobility of such dislocation loops was demonstrated in a recent *in situ* transmission electron microscopy study,⁶³ where a nanometer-

sized dislocation loop in α -Fe was shown to undergo an active thermally activated one-dimensional diffusion at a temperature as low as 575 K.

Indeed, although the temperature at the depth of the location of the interstitial and the cluster of interstitials drops down to ~ 1100 K ($\sim 0.46T_m$) by the end of the simulation, both the interstitial and the cluster remain very mobile, as can be seen from changes in the positions and orientations of the $\langle 110 \rangle$ -dumbbell interstitial and the four $\langle 111 \rangle$ -crowdion cluster in Fig. 8. The mechanisms of interstitial diffusion observed in MD simulations performed for different bcc metals include reorientation of the $\langle 110 \rangle$ dumbbell in one of the $\langle 111 \rangle$ directions followed by low-energy barrier jumps along the close-packed $\langle 111 \rangle$ direction,^{60,64} as well as rotation and translation of $\langle 110 \rangle$ dumbbell.^{55,65} While the mobility of the interstitials and their clusters at low temperatures can be strongly affected by relatively small variations in the values of the energy barriers separating different self-interstitial configurations, at high temperatures realized in our simulations ($T \sim 1100$ – 2650 K; $k_B T \sim 0.1$ – 0.2 eV) different types of jumps and reorientations of the interstitial configurations can be readily activated, making the diffusion pathways more complex^{59,66} and, at the same time, less sensitive to the detailed energy landscape predicted with a particular interatomic potential.

The high mobility of the interstitial cluster observed in Fig. 8 is consistent with the decrease in the migration energy with increasing cluster size reported in MD simulations performed with different interatomic potentials.^{61,62,64,65} The diffusion of a small interstitial cluster is typically described as a combination of a rapid one-dimensional migration along the crowdion direction and rotations to the equivalent $\langle 111 \rangle$ directions. The frequency of the rotations is increasing with temperature and decreasing with the size of the cluster.^{61,62,64,65} For the cluster of four interstitials observed in the present simulation, the temperature of the surface region of the target remains sufficiently high during the time of the simulation to induce occasional reorientations of the cluster, resulting in a three-dimensional migration of the cluster (Fig. 8).

The high mobility of the remaining interstitial and the interstitial cluster suggests that they are likely to recombine with vacancies or escape to the surface as the cooling process continues. The positions of the vacancies, on the other hand, become relatively static by the end of the simulation. The distribution of vacancies in the top 8 nm surface region of the target is shown in Fig. 9. There is a total of 53 vacancies in this region, with three more vacancies located below the region shown in the plot at 10.3, 11.2, and 15.1 nm below the surface. Despite the high concentration of vacancies in the surface region of the target (1.7×10^{-3} in a layer between 1 and 5 nm below the surface), we do not observe any tendency of vacancies to form clusters or small dislocation loops. Only three pairs of vacancies occupying adjacent second-nearest-neighbor lattice sites; one pair in fourth-nearest-neighbor lattice sites and one pair in fifth-nearest-neighbor lattice sites have been identified at 500 ps after the laser pulse. The absence of any pronounced clustering of vacancies can be explained by relatively low (as compared to clusters of interstitials) binding energies of divacancies and

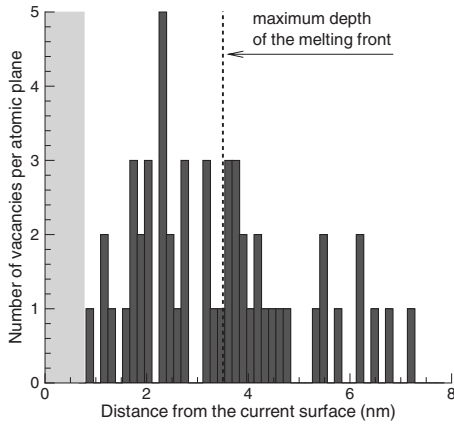


FIG. 9. Distribution of vacancies in the top 8 nm surface region of a bulk Cr target irradiated with a 200 fs laser pulse at an absorbed fluence of 638 J/m^2 at 500 ps after the laser pulse. The width of an individual bar in the histogram corresponds to the distance between (001) planes, with each bar showing the number of vacancies in an individual (001) atomic plane. The gray area in the left part of the figure corresponds to the surface layer where identification of vacancies is not possible. The dashed line marks the depth of the region that experiences a transient melting and resolidification during the first 85 ps of the simulation.

larger vacancy clusters,^{55,59,61,62} as well as by the high temperature of the surface region of the irradiated target during the time of the simulation (Fig. 4).

The fact that a large fraction of the vacancies (52% at 500 ps) are located in the part of the target that experienced a transient melting and resolidification (Fig. 9) suggests that, in addition to the thermally activated generation of vacancy-interstitial pairs, a significant number of vacancies can be left behind by the quickly advancing solidification front. The lattice distortions associated with the transient laser-induced stresses and the quasistatic uniaxial thermal expansion of the surface region may also affect the elementary processes responsible for the generation and mobility of the point defects.⁶⁷ A more detailed analysis of the relative contribution of different factors to the generation and evolution of the defect structures in short pulse laser processing is the subject of our ongoing work.

D. Long-term evolution of the vacancy configuration

To evaluate the possible long-term evolution of the vacancies generated in the surface region of the irradiated target, we calculate the diffusivity of a vacancy and estimate the characteristic diffusion length of a vacancy during the cooling process. The diffusion coefficient of a vacancy, D_v , is calculated based on a series of MD simulations performed for bcc crystals containing a single vacancy at several temperatures in the range from 1000 to 1500 K. The diffusion coefficient for each temperature is calculated using the Einstein relation, $D_v = (1/6t) \langle |\vec{R}_i(t_0+t) - \vec{R}_i(t_0)|^2 \rangle_{i,t_0}$, where $\vec{R}_i(t)$ is the vacancy position at time t in the i th simulation. The averaging over starting times t_0 along the MD trajectories is used to improve statistical accuracy of the calculation. Fitting the values of the diffusion coefficient obtained for dif-

ferent temperatures to the Arrhenius dependence, $D_v(T) = D_v^0 \exp(-E_v^m/k_B T)$, yields the vacancy migration energy $E_v^m = 0.81 \text{ eV}$ and the pre-exponential factor $D_v^0 = 0.39 \times 10^{-2} \text{ cm}^2/\text{s}$. The value of the migration energy predicted with the EAM Cr potential is higher than the values of 0.70 (Ref. 27) and 0.73 eV (Ref. 29) predicted with MEAM Cr potentials but is somewhat lower than the value of 0.91 eV evaluated in DFT calculations⁵⁷ and the experimental value of 0.95 eV.³²

The knowledge of the vacancy diffusivity at different temperatures allows us to back calculate the vacancy jump rates. For random thermally activated jumps to the nearest-neighbor lattice sites, the jump rate can be calculated as $1/\tau = 6D_v/r_1^2 = 8D_v/a^2$, where $r_1 = \sqrt{3}/4a$ is the nearest-neighbor distance in the bcc lattice and τ is the characteristic time between jumps of a vacancy. For the surface temperature of 1180 K predicted in the TTM-MD simulation for 500 ps after the laser pulse (Fig. 4), the above equation gives $1/\tau = 37 \text{ GHz}$, or $\tau = 27 \text{ ps}$, explaining the slow pace of changes in the vacancy configuration observed during the last hundred picoseconds of the simulation.

To extend the estimations beyond the duration of the TTM-MD simulation, we take the temperature profile predicted at the end of the simulation, 500 ps after the laser pulse, and follow the further temperature evolution in the target by numerically solving a one-dimensional heat conduction equation in a wide region of the target extending up to $10 \mu\text{m}$, where the temperature is fixed at 300 K. All the active exothermic or endothermic structural transformations in the surface region of the target are ceased by 500 ps, making the description of the long-term temperature evolution by the heat conduction equation adequate. A contribution of the heat conduction in the radial directions can be expected to increase with time and the cooling rate predicted by the one-dimensional heat conduction equation can be considered to be the lower-end estimate corresponding to the infinitely large laser spot size. The solution of the heat conduction equation predicts that the surface temperature drops down to 900 K by 835 ps, 700 K by 1.65 ns, 500 K by 6.1 ns, and 350 K by 95 ns after the laser pulse, as shown in Fig. 10.

The knowledge of the temperature evolution in the surface region of the target and the temperature dependence of the vacancy diffusion coefficient allows us to predict the extent of the rearrangements the vacancy configuration generated by the end of the TTM-MD simulation would undergo during the remaining part of the cooling process. The root-mean-square displacement of vacancies during the cooling process can be estimated by integrating the Einstein relation over the cooling time, with the result of the integration shown in Fig. 10. The average diffusion length traveled by a vacancy increases during the time from 0.5 to 1.5 ns and saturates at later times at a level not exceeding 0.33 nm. The saturation of the vacancy diffusion length occurs when the temperature drops below 700 K and the vacancy diffusion coefficient, D_v , drops below $10^{-8} \text{ cm}^2/\text{s}$. The relatively small, on the order of an interatomic distance, vacancy diffusion length after 500 ps suggests that the configuration of mostly individual vacancies observed at the end of the TTM-MD simulation (Fig. 8) is unlikely to undergo any significant changes during the remaining part of the cooling process.

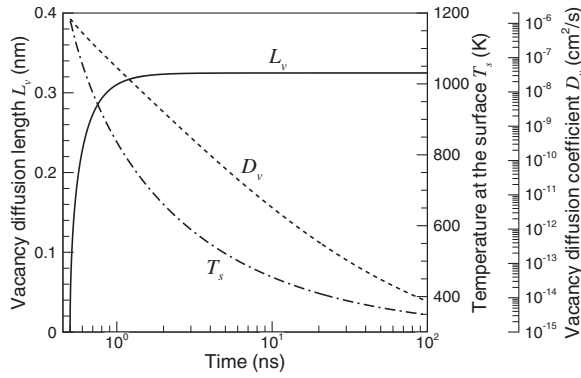


FIG. 10. Long-term evolution of the surface temperature, vacancy diffusion coefficient, and vacancy diffusion length (root-mean-square displacement of vacancies) in the surface region of a bulk Cr target irradiated with a 200 fs laser pulse at an absorbed fluence of 638 J/m^2 during the late stage of the cooling process, starting from 500 ps after the laser pulse. The temperature is obtained by numerical integration of the heat conduction equation, starting from the temperature profile predicted in the TTM-MD simulation at the time of 500 ps. Surface temperature variation during the first 500 ps is shown in Fig. 4.

The high supersaturation of the surface region of the target with vacancies can lead to slow atomic rearrangements and eventual vacancy clustering at longer times. Indeed, the binding energies of compact three-dimensional clusters⁶² and vacancy loops^{61,68} increase with the cluster size and the stability of the clusters increases with decreasing temperature. The formation of vacancy clusters can be accelerated by annealing at an elevated temperature or by reheating of the target in the multipulse laser irradiation regime. The long-term structural evolution of the surface region is defined by the mobility of vacancy clusters that is not fully understood at this time⁶⁹ and depends on the types of the clusters. In particular, the vacancy clusters can transform into small glissile dislocation loops exhibiting one-dimensional thermally activated motion^{61,63} or can become immobile compact/spherical nanovoids.⁶²

The accumulation of vacancies and vacancy clusters, as well as the generation of nanovoids in multipulse irradiation regime may weaken the material and result in the incubation effect, when the laser fluence threshold for ablation/damage decreases significantly with increasing number of laser pulses applied to the same area.^{70–74} In particular, the generation of subsurface defects may reduce the ability of material to withstand the dynamic loading associated with the laser-induced stress wave [Fig. 3(b)], leading to the decrease in the fluence threshold for photomechanical spallation¹⁴ of the target in the multipulse irradiation regime. The decreased stability of the surface region supersaturated with vacancies against melting^{44,75,76} may result in the increase in the depth of the region affected by the transient melting and, in turn, facilitate generation of the higher densities of the surface defects by subsequent laser pulses. The effect of the vacancy generation may also be turned to a useful account, providing avenues for controlled redistribution/incorporation of impurities or mixing/alloying in multicomponent/composite targets.

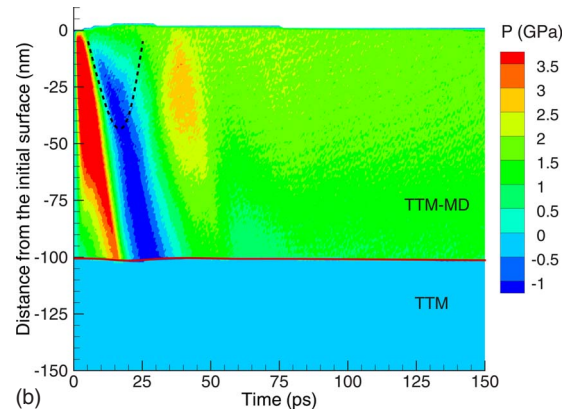
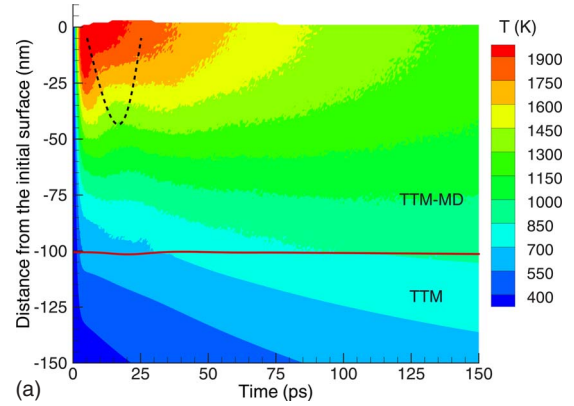


FIG. 11. (Color online) Contour plots of the spatial and temporal evolution of (a) temperature and (b) pressure in a TTM-MD simulation of a bulk Cr target irradiated with a 200 fs laser pulse at an absorbed fluence of 425 J/m^2 . Laser pulse is directed along the Y axes from the top of the contour plots. The red solid line separates the continuum (TTM) and atomistic (TTM-MD) parts of the computational system. The black dashed line marks the depth of the region where stacking faults are observed.

E. Simulation at laser fluence below the threshold for surface melting

To study the effect of the laser fluence on the structural changes in the surface region of the target, an additional simulation has been performed at a lower fluence of 425 J/m^2 . The overall picture of the evolution of the lattice temperature and pressure in the surface region of the target (Fig. 11) is similar to the one discussed above for the higher fluence (Fig. 3). The maximum temperature of 2140 K, reached at the surface of the target at 5 ps, however, is below the equilibrium melting temperature of the model EAM Cr material, 2381 K, and no surface melting takes place. The lower temperatures result in the lower levels of the compressive and tensile stresses, with the latter does not exceeding -1.5 GPa .

Similarly to the higher-fluence simulation discussed above, the expansion of the lattice associated with the unloading tensile wave causes multiple internal shifts in the surface region of the target and generation of stacking faults along the $\{110\}$ planes (Fig. 12). The depth of the region where the stacking faults are observed in this simulation,

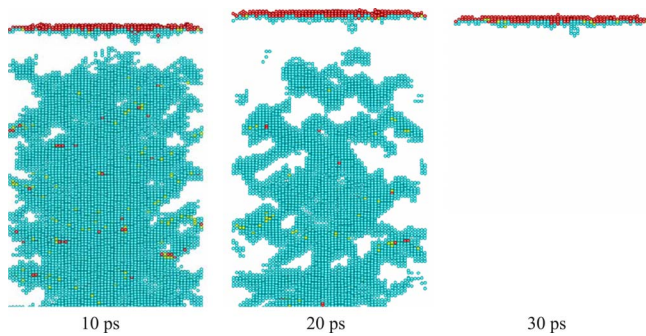


FIG. 12. (Color online) Snapshots of the surface regions of atomic configurations obtained in a TTM-MD simulation of a bulk Cr target irradiated with a 200 fs laser pulse at an absorbed fluence of 425 J/m^2 . The snapshots are taken along the $[\bar{1}\bar{1}0]$ view direction and are shown down to the depth of 15 nm below the level of the initial surface. The configurations are quenched to 0 K in order to reduce thermal noise in atomic positions and energies. The same coloring scheme as in Figs. 5 and 8 is used here, with atoms that have energies below -3.99 eV blanked to expose crystal defects.

however, does not exceed 45 nm and the stacking faults quickly disappear as soon as the tensile stress wave leaves the surface region of the target. Visual analysis of the snapshots of atomic configurations, shown in Fig. 12, indicates that the stacking faults completely disappear by 30 ps. Moreover, not a single point defect is generated in this simulation. This observation suggests that the generation of stable crystal defects and possible accumulation of damage in multipulse irradiation regime, discussed above for the higher-fluence simulation, take place only at or above the threshold fluence for surface melting.

V. SUMMARY

A detailed analysis of the structural changes in a surface region of a bcc Cr target irradiated by a femtosecond laser pulse is performed based on the results of large-scale atomic-level simulations. The simulations are enabled by the development of EAM potential for Cr, which provides a computationally efficient yet sufficiently accurate description of the structural and thermodynamic properties of the real Cr. Some of the parameters of the model EAM Cr material, such as vacancy migration energy, temperature dependence of the elastic moduli, and the equilibrium melting temperature, are calculated and related to experimental data and predictions of DFT calculations. A description of the laser excitation of conduction-band electrons, electron-phonon coupling, and electron heat conduction in the irradiated target is included in the computational model by incorporating a continuum description of the evolution of the electron temperature into the atomistic MD method.

A combined effect of the fast temperature variation and strong thermoelastic stresses produced by the laser energy deposition causes both transient structural changes and the generation of permanent crystal defects in the surface region

of the irradiated target. The transient structural changes include fast surface melting and resolidification, as well as the generation of a high density of stacking faults along the $\{110\}$ planes. At an absorbed laser fluence of 638 J/m^2 , the surface melting and subsequent epitaxial resolidification affect only a thin $\sim 3.5 \text{ nm}$ layer of the target and the resolidification process is completed by the time of 85 ps after the laser pulse. The stacking faults appear as a result of internal shifts in the crystal undergoing a rapid uniaxial expansion in the direction normal to the irradiated surface. The growth of the region where the stacking faults are observed follows closely the propagation of the tensile component of the laser-induced stress wave. The stacking faults are unstable and quickly disappear when the tensile stress wave leaves the surface region and the lattice deformation partially relaxes.

An important prediction of the simulations is that a high concentration of vacancies, on the order of 10^{-3} per lattice site, can be produced in the surface region of the irradiated target at laser fluences close or above the surface melting threshold. The thermally activated generation of vacancy-interstitial pairs during the laser-induced temperature spike, when the crystalline part of the target can be transiently overheated up to more than 20% above the equilibrium melting temperature,^{12,46,51,77} serves as the initial source of the point defects. Due to the high mobility of self-interstitials, they quickly escape to the melting front or the free surface of the target, leaving behind a large number of vacancies. A significant number of vacancies can also be produced at the advancing solid-liquid interface during the fast resolidification process. The strong temperature gradient created in the surface region of the target by femtosecond laser irradiation and associated ultrafast cooling rates exceeding $5 \times 10^{12} \text{ K/s}$ at the time of resolidification (Fig. 4) provide the conditions for stabilization of the highly nonequilibrium vacancy concentration. The cooling rate, together with the original microstructure and presence of impurities, controls the long-term evolution of the defect structures.

The generation of vacancies and vacancy clusters may result in damage accumulation, generation of nanovoids, and degradation of the mechanical properties of the surface region of the target in the multipulse irradiation regime. The generation of crystal defects may be, thus, related to the incubation effect observed in laser ablation and damage.⁷⁰⁻⁷⁴ The high density of vacancies generated in the surface region should also play an important role in redistribution of impurities or mixing/alloying in multicomponent or composite targets. The small depth of the region where the defects are generated may provide avenues for controlled nanoscale modification of material properties.

ACKNOWLEDGMENTS

Financial support of this work was provided by the National Science Foundation through the Thermal Transport and Thermal Processes Program of the Chemical, Bioengineering, Environmental, and Transport Systems Division (Grant No. CTS-0348503).

- *Author to whom correspondence should be addressed. lz2n@virginia.edu
- ¹M. von Allmen and A. Blatter, *Laser Beam Interactions with Materials* (Springer, Berlin, 1998).
 - ²D. Bäuerle, *Laser Processing and Chemistry* (Springer-Verlag, Berlin, 2000).
 - ³J. Kaspar and A. Luft, *Surf. Eng.* **17**, 379 (2001).
 - ⁴J. G. Hoekstra, S. B. Quadri, J. R. Scully, and J. M. Fitz-Gerald, *Adv. Eng. Mater.* **7**, 805 (2005).
 - ⁵R. Le Harzic, N. Huot, E. Audouard, C. Jonin, P. Laporte, S. Valette, A. Fraczkiewicz, and R. Fortunier, *Appl. Phys. Lett.* **80**, 3886 (2002).
 - ⁶V. Margetic, K. Niemax, and R. Hergenröder, *Anal. Chem.* **75**, 3435 (2003).
 - ⁷Q. Feng, Y. N. Picard, H. Liu, S. M. Yalisove, G. Mourou, and T. M. Pollock, *Scr. Mater.* **53**, 511 (2005).
 - ⁸T. H. R. Crawford, J. Yamanaka, G. A. Botton, and H. K. Haugen, *J. Appl. Phys.* **103**, 053104 (2008).
 - ⁹D. S. Ivanov, B. C. Rethfeld, G. M. O'Connor, T. J. Glynn, A. N. Volkov, and L. V. Zhigilei, *Appl. Phys. A: Mater. Sci. Process.* (to be published).
 - ¹⁰X. W. Wang, *J. Phys. D* **38**, 1805 (2005).
 - ¹¹D. S. Ivanov and L. V. Zhigilei, *Phys. Rev. B* **68**, 064114 (2003).
 - ¹²D. S. Ivanov and L. V. Zhigilei, *Phys. Rev. Lett.* **91**, 105701 (2003).
 - ¹³Z. Lin and L. V. Zhigilei, *Phys. Rev. B* **73**, 184113 (2006).
 - ¹⁴E. Leveugle, D. S. Ivanov, and L. V. Zhigilei, *Appl. Phys. A: Mater. Sci. Process.* **79**, 1643 (2004).
 - ¹⁵L. V. Zhigilei, D. S. Ivanov, E. Leveugle, B. Sadigh, and E. M. Bringa, *Proc. SPIE* **5448**, 505 (2004).
 - ¹⁶E. Ohmura, I. Fukumoto, and I. Miyamoto, *Int. J. Jpn. Soc. Precis. Eng.* **32**, 248 (1998).
 - ¹⁷C. Schäfer, H. M. Urbassek, and L. V. Zhigilei, *Phys. Rev. B* **66**, 115404 (2002).
 - ¹⁸N. N. Nedialkov, S. E. Imamova, and P. A. Atanasov, *J. Phys. D* **37**, 638 (2004).
 - ¹⁹C. Cheng and X. Xu, *Phys. Rev. B* **72**, 165415 (2005).
 - ²⁰M. B. Agranat, S. I. Anisimov, S. I. Ashitkov, V. V. Zhakhovskii, N. A. Inogamov, K. Nishihara, Yu. V. Petrov, V. E. Fortov, and V. A. Khokhlov, *Appl. Surf. Sci.* **253**, 6276 (2007).
 - ²¹S. I. Anisimov, B. L. Kapeliovich, and T. L. Perel'man, *Sov. Phys. JETP* **39**, 375 (1974).
 - ²²L. V. Zhigilei and B. J. Garrison, in *Multiscale Modelling of Materials*, MRS Symposia Proceedings No. 538 (Materials Research Society, Pittsburgh, 1999), pp. 491–496.
 - ²³C. Schäfer, H. M. Urbassek, L. V. Zhigilei, and B. J. Garrison, *Comput. Mater. Sci.* **24**, 421 (2002).
 - ²⁴C. Kittel, *Introduction to Solid State Physics*, 7th ed. (Wiley, New York, 1996).
 - ²⁵S. D. Brorson, A. Kazeroonian, J. S. Moodera, D. W. Face, T. K. Cheng, E. P. Ippen, M. S. Dresselhaus, and G. Dresselhaus, *Phys. Rev. Lett.* **64**, 2172 (1990).
 - ²⁶*Handbook of Optical Constants of Solids I*, edited by D. Palik (Academic, London, 1985); *Handbook of Optical Constants of Solids II*, edited by D. Palik (Academic, London, 1991).
 - ²⁷B. J. Lee, M. I. Baskes, H. Kim, and Y. K. Cho, *Phys. Rev. B* **64**, 184102 (2001).
 - ²⁸R. Pasianot, D. Farkas, and E. J. Savino, *Phys. Rev. B* **43**, 6952 (1991).
 - ²⁹B. Zhang, Y. Ouyang, S. Liao, and Z. Jin, *Physica B (Amsterdam)* **262**, 218 (1999).
 - ³⁰R. A. Johnson and D. J. Oh, *J. Mater. Res.* **4**, 1195 (1989).
 - ³¹X. W. Zhou, H. N. G. Wadley, R. A. Johnson, D. J. Larson, N. Tabat, A. Cerezo, A. K. Petford-Long, G. D. W. Smith, P. H. Clifton, R. L. Martens, and T. F. Kelly, *Acta Mater.* **49**, 4005 (2001).
 - ³²P. Ehrhart, P. Jung, H. Schulta, and H. Ullmaier, in *Atomic Defects in Metals*, Landolt-Börnstein, New Series, Group III, Vol. 25, edited by H. Ullmaier (Springer-Verlag, Berlin, 1991).
 - ³³D. I. Bolef and J. de Klerk, *Phys. Rev.* **129**, 1063 (1963).
 - ³⁴J. R. Ray and A. Rahman, *J. Chem. Phys.* **80**, 4423 (1984).
 - ³⁵T. Çağın, G. Dereli, M. Uludoğan, and M. Tomak, *Phys. Rev. B* **59**, 3468 (1999).
 - ³⁶M. Karimi, G. Stapy, T. Kaplan, and M. Mostoller, *Modell. Simul. Mater. Sci. Eng.* **5**, 337 (1997).
 - ³⁷K. Yoshimoto, G. J. Papakonstantopoulos, J. F. Lutsko, and J. J. de Pablo, *Phys. Rev. B* **71**, 184108 (2005).
 - ³⁸K. W. Katahara, M. Nimalendran, M. H. Manghnani, and E. S. Fisher, *J. Phys. F: Met. Phys.* **9**, 2167 (1979).
 - ³⁹*Smithells Metal Reference Book*, 7th ed., edited by E. A. Brandes and G. B. Brook (Butterworth-Heinemann, Oxford, 1998).
 - ⁴⁰J.-O. Andersson, *Int. J. Thermophys.* **6**, 411 (1985).
 - ⁴¹G. K. White and C. Andrikidis, *Phys. Rev. B* **53**, 8145 (1996).
 - ⁴²M. Born, *J. Chem. Phys.* **7**, 591 (1939).
 - ⁴³J. Wang, J. Li, S. Yip, S. Phillpot, and D. Wolf, *Phys. Rev. B* **52**, 12627 (1995).
 - ⁴⁴V. Sorkin, E. Polturak, and J. Adler, *Phys. Rev. B* **68**, 174102 (2003).
 - ⁴⁵Z. H. Jin, P. Gumbsch, K. Lu, and E. Ma, *Phys. Rev. Lett.* **87**, 055703 (2001).
 - ⁴⁶S. N. Luo, T. J. Ahrens, T. Çağın, A. Strachan, W. A. Goddard, and D. C. Swift, *Phys. Rev. B* **68**, 134206 (2003).
 - ⁴⁷The use of terms “lattice” and “lattice temperature” in this paper does not imply the preservation of the crystalline order in the system. By using these terms we merely follow the terminology established in the literature presenting TTM calculations, when the term lattice temperature is commonly used to refer to the temperature of the ionic subsystem that can be brought out of equilibrium with the conduction-band electrons by short pulse irradiation or high-energy ion bombardment.
 - ⁴⁸M. Forsblom and G. Grimvall, *Phys. Rev. B* **72**, 054107 (2005).
 - ⁴⁹X.-M. Bai and M. Li, *Phys. Rev. B* **77**, 134109 (2008).
 - ⁵⁰W. H. Duff and L. V. Zhigilei, *J. Phys.: Conf. Ser.* **59**, 413 (2007).
 - ⁵¹D. S. Ivanov and L. V. Zhigilei, *Phys. Rev. Lett.* **98**, 195701 (2007).
 - ⁵²J. B. Cohen, R. Hinton, K. Lay, and S. Sass, *Acta Metall.* **10**, 894 (1962).
 - ⁵³V. Vitek, *Philos. Mag.* **18**, 773 (1968).
 - ⁵⁴V. Vitek, *Philos. Mag.* **21**, 1275 (1970).
 - ⁵⁵R. A. Johnson, *Phys. Rev.* **134**, A1329 (1964).
 - ⁵⁶G. J. Ackland and R. Thetford, *Philos. Mag. A* **56**, 15 (1987).
 - ⁵⁷D. Nguyen-Manh, A. P. Horsfield, and S. L. Dudarev, *Phys. Rev. B* **73**, 020101(R) (2006).
 - ⁵⁸P. Olsson, J. Wallenius, C. Domain, K. Nordlund, and L. Malerba, *Phys. Rev. B* **72**, 214119 (2005).
 - ⁵⁹P. M. Derlet, D. Nguyen-Manh, and S. L. Dudarev, *Phys. Rev. B* **76**, 054107 (2007).
 - ⁶⁰B. D. Wirth, G. R. Odette, D. Maroudas, and G. E. Lucas, *J. Nucl. Mater.* **244**, 185 (1997).

- ⁶¹Yu. N. Osetsky, D. J. Bacon, A. Serra, B. N. Singh, and S. I. Golubov, *J. Nucl. Mater.* **276**, 65 (2000).
- ⁶²N. Soneda and T. D. de la Rubia, *Philos. Mag. A* **78**, 995 (1998).
- ⁶³K. Arakawa, K. Ono, M. Isshiki, K. Mimura, M. Uchikoshi, and H. Mori, *Science* **318**, 956 (2007).
- ⁶⁴N. Soneda and T. Diaz de La Rubia, *Philos. Mag. A* **81**, 331 (2001).
- ⁶⁵D. A. Terentyev, L. Malerba, and M. Hou, *Phys. Rev. B* **75**, 104108 (2007).
- ⁶⁶R. C. Pasianot, A. M. Monti, G. Simonelli, and E. J. Savino, *J. Nucl. Mater.* **276**, 230 (2000).
- ⁶⁷F. Gao, D. J. Bacon, P. E. J. Flewitt, and T. A. Lewis, *Nucl. Instrum. Methods Phys. Res. B* **180**, 187 (2001).
- ⁶⁸V. G. Kapinos, Yu. N. Osetskii, and P. A. Platonov, *J. Nucl. Mater.* **173**, 229 (1990).
- ⁶⁹B. D. Wirth, *Science* **318**, 923 (2007).
- ⁷⁰D. Ashkenasi, M. Lorenz, R. Stoian, and A. Rosenfeld, *Appl. Surf. Sci.* **150**, 101 (1999).
- ⁷¹P. T. Mannion, J. Magee, E. Coyne, G. M. O'Connor, and T. J. Glynn, *Appl. Surf. Sci.* **233**, 275 (2004).
- ⁷²S. E. Kirkwood, A. C. van Popta, Y. Y. Tsui, and R. Fedosejevs, *Appl. Phys. A: Mater. Sci. Process.* **81**, 729 (2005).
- ⁷³J. Krüger, D. Dufft, R. Koter, and A. Hertwig, *Appl. Surf. Sci.* **253**, 7815 (2007).
- ⁷⁴G. Raciukaitis, M. Brikas, P. Gecys, and M. Gedvilas, *Proc. SPIE* **7005**, 7005 (2008).
- ⁷⁵T. Górecki, *Z. Metallkd.* **65**, 426 (1974).
- ⁷⁶T. Górecki, *Scr. Metall.* **11**, 1051 (1977).
- ⁷⁷A. B. Belonoshko, N. V. Skorodumova, A. Rosengren, and B. Johansson, *Phys. Rev. B* **73**, 012201 (2006).